Droplet ejection by spring-like elastic pillars

Huanhuan Zhang[1,2,#], Wei Zhang[1,2,#], Yuankai Jin[2,#], Chenyang Wu[2,#], Zhenyu Xu[2], Siyan Yang[1,2], Shouwei Gao[1,2], Fayu Liu[1,2], Wanghuai Xu[1], Steven Wang[2], Haimin Yao[1,*], Zuankai Wang[1,*]

[1]Department of Mechanical Engineering, The Hong Kong Polytechnic University, Hong Kong 999077, China.

[2]Department of Mechanical Engineering, City University of Hong Kong, Hong Kong 999077, China.

[#] These authors contributed equally to this work.

*Corresponding authors: mmhyao@polyu.edu.hk, (H. Y.); zk.wang@polyu.edu.hk, (Z. W.).

Abstract

Preventing the accretion of water droplets on surfaces is fundamentally interesting and practically important. It has been demonstrated that water droplets staying at room temperature can spontaneously detach from surfaces through texture design or coalescence-induced surface-to-kinetic energy transformation. However, under freezing conditions, these strategies become ineffective owing to the manifestation of stronger droplet-surface interaction and the lack of the pathway for energy transformation. Here, leveraging the water volume expansion during the freezing process, we report a rationally designed structured elastic surface (SES) with spring-like pillars and wetting contrast that renders the spontaneous ejection of freezing water droplets, regardless of their impacting locations. We demonstrate that the work done by the seconds-long, gradual volume expansion of freezing droplets can be stored as elastic energy in the spring-like pillar and then rapidly released as kinetic energy within milliseconds. The three-orders-of-magnitude reduction in timescales between the two energy transformation processes leads to sufficient kinetic energy to drive freezing droplet ejection. We also build a theoretical modeling to elucidate the determining factors for the successful onset of this phenomenon. Our design is also scalable in manufacturing, opening up applications in de-icing, soft robotics, and power generation.

Main

Timely and spontaneous removal of droplets from surfaces has long been a hot pursuit in many practical applications such as energy harvesting[1], thermal management[2], self-cleaning[3], and anti-icing[4,5]. Fueled by evolutionary innovations, nature has mastered this skill, as exemplified by the repelling of water droplets on lotus leaves[6], pitcher plants[7,8], and cicada wings[9], as well as the shedding of sticky honeydew droplets on galling aphids[10]. Over the past decade, extensive efforts have been made to develop nature-inspired surfaces[3,8,11], on which water droplets staying in above-freezing conditions can be instantly removed via the utilization of surface energy, such as coalescence-induced jumping[9,12] and bouncing[11,13-16] (Fig. 1a). But such surface energy-driven strategies become ineffective for freezing water droplets in sub-zero environments. This is because, in striking contrast to water droplets at room temperature, the freezing droplets have a much stronger adhesion to underlying surfaces, and the formation of ice shell prevents the coalescence of droplets for surface energy release.

Modifying surfaces with proper wettability[17-19], stiffness[20,21], or slipperiness[4,22-24] can delay ice nucleation and propagation or reduce ice adhesion [25-28]; however, external energy is still needed to remove freezing droplets before they accrete into large ice films. For example, under vacuum conditions, droplets freezing on superhydrophobic surfaces can exhibit self-expulsion behavior by leveraging the explosive and asymmetric release of latent heat to generate a recalescence force to overcome the surface adhesion[29]. However, at atmospheric pressure, where the recalescence force becomes negligible compared to the adhesion force, the freezing droplets remain adhered to the underlying surfaces instead of being expelled[29]. The accretion of freezing droplets and icing can lead to detrimental impact, as evidenced by the disaster in Texas, U.S., in 2021 that disrupted high-speed roads and power lines and put millions of families and factories into desperation. To date, achieving freezing droplet self-removal from surfaces remains challenging, in spite of recent advances in understanding freezing dynamics from the nucleus level to the film level[30-33].

One simple yet easily neglected fact is that the freezing of water naturally leads to ~9% volume expansion under normal atmospheric conditions[34], which might serve as an alternative energy source for droplet ejection. Previously, it has been shown that the volume expansion work done by a small volume of freezing water can produce high local pressure that even fractures brittle cast iron, known as “freezing bomb”[34]. However, owing to the slow freezing process, utilizing the volume expansion work to dynamically render the spontaneous ballistic ejection of droplets is more challenging than statically fracturing cast iron. Although previous

efforts have successfully utilized the volume expansion effect to achieve self-dislodging of freezing droplets on superhydrophobic surfaces, the self-dislodging freezing droplets exhibit limited motility under atmospheric conditions[19], highlighting the challenges in utilizing volume expansion work to drive droplet ejection.

To accelerate the energy transformation to drive freezing droplet ejection, we conceive that by the rational design of a structured elastic surface, termed SES, it is possible to first convert the freezing droplet's volume expansion work into the elastic energy stored in the SES (Stage I) and then into the kinetic energy of the freezing droplet in a rapid manner (Stage II) (Fig. 1b, Supplementary Video 1). One intriguing analogous example achieving such an elastic-to-kinetic energy transformation is the fungus *Pilobolus kleinii,* which can spontaneously disperse spores (Extended Data Fig. 1)[35]. Briefly, its vesicle stores elastic energy via the absorption of ambient moisture. Once a critical internal pressure is reached, the vesicle explodes and instantaneously releases the stored elastic energy, ballistically discharging the spores at its tip[35].

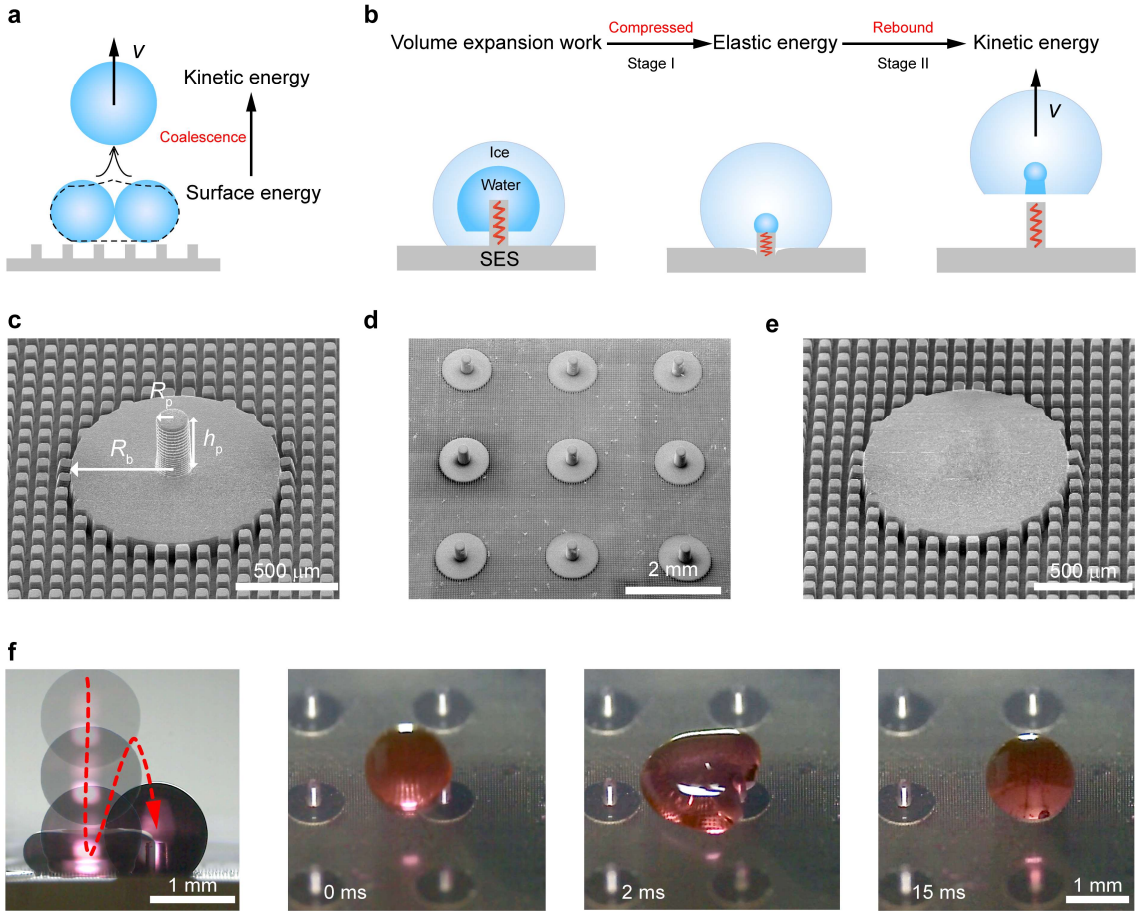

Fig. 1 | Design of the structured elastic surface. a, Schematics showing water droplet ejection driven by the surface energy released from the coalescence of two contacting droplets. **b,**

Conception of freezing droplet ejection on a structured elastic surface (SES) that can harness the volume expansion work of the freezing droplet through a two-stage energy conversion process. **c,** Scanning electron microscope (SEM) image showing the structures of the SES, consisting of a pillar with a radius of R_p and a height of h_p, a smooth base with a radius R_b, and a micro-patterned substrate surrounding the base. **d,** SEM image of the SES arrays. **e,** SEM image showing the non-structured surface as a control sample. **f,** Optical images showing the automatic positioning of a randomly released droplet onto a pillar on the SES arrays.

Fig. 1c shows a representative SES that consists of three key components: a smooth base with a radius R_b = 0.5 mm, a deformable spring-like pillar with a radius R_p = 0.09 mm and a height h_p = 0.4 mm located at the center of the base, and a micro-patterned substrate surrounding the base (Fig. 1c). The SES is made of elastic polydimethylsiloxane (PDMS) through a simple cast-molding process (Extended Data Fig. 2), allowing the scalable production as evidenced by the SES arrays in Fig. 1d. Moreover, we can easily tailor the compressive modulus K_c of the SES through the mixing ratio of base to cross-linker of PDMS (Extended Data Fig. 3 and Extended Data Table 1). We also prepared two control samples, namely a non-structured sample without the pillar structure (Fig. 1e) and a stiffer sample with a larger K_c. Note that owing to the intrinsic hydrophobicity of PDMS, the contact angle of a water droplet on the micro-patterned substrate is amplified to ~160°, indicating the superhydrophobicity of the micro-patterned substrate (Extended Data Fig. 4). The wettability contrast between the hydrophobic smooth base and the superhydrophobic micro-patterned substrate of SES could drive randomly impacting droplets to spontaneously move to the smooth base and be captured by the spring-like pillar, which facilitates the scalability and practicality. As shown in Fig. 1f, a water droplet impacting the SES arrays spreads and contacts with a nearby pillar, retracts asymmetrically towards the pillar, and finally settles on top of it.

Fig. 2 compares the behaviors of droplets freezing on the SES and the two control samples. To mimic the natural freezing condition, we conducted the experiments in a customized isothermal chamber (Extended Data Fig. 5), where the droplet is cooled down by the circulated cold air at -15℃ rather than the underlying substrate, as shown by the thermographic imaging, (Extended Data Fig. 6, Supplementary Video 2). The isothermal condition allows droplets to freeze in an "outside-in" mode. On the SES sample with $R_b = 0.5$ mm and $K_c = 1.7$ MPa, a 1-μL water droplet gradually freezes in the first 5 s and is suddenly ejected away at 5.752 s (Fig. 2a). By recording the ejection process at 10,000 fps, we found that the compressed spring-

like pillar rapidly bounces up within 0.2 ms, which likely gives rise to sufficient force and energy for freezing droplet ejection (Fig. 2b). The ejecting trajectory deviates from the vertical direction, which is mainly attributed to the non-perfectly symmetrical geometry and freezing process of the droplet in practice. Such a non-vertical trajectory enables the droplet to escape from the surface rather than return to the original launching site. By contrast, for the non-structured or stiffer samples, the 1-μL droplets completely freeze and stick to these surfaces (Fig. 2 c and d). Such contrastive phenomena suggest that the pillar structure and the stiffness of SES are essential for achieving the spontaneous ejection of freezing droplets.

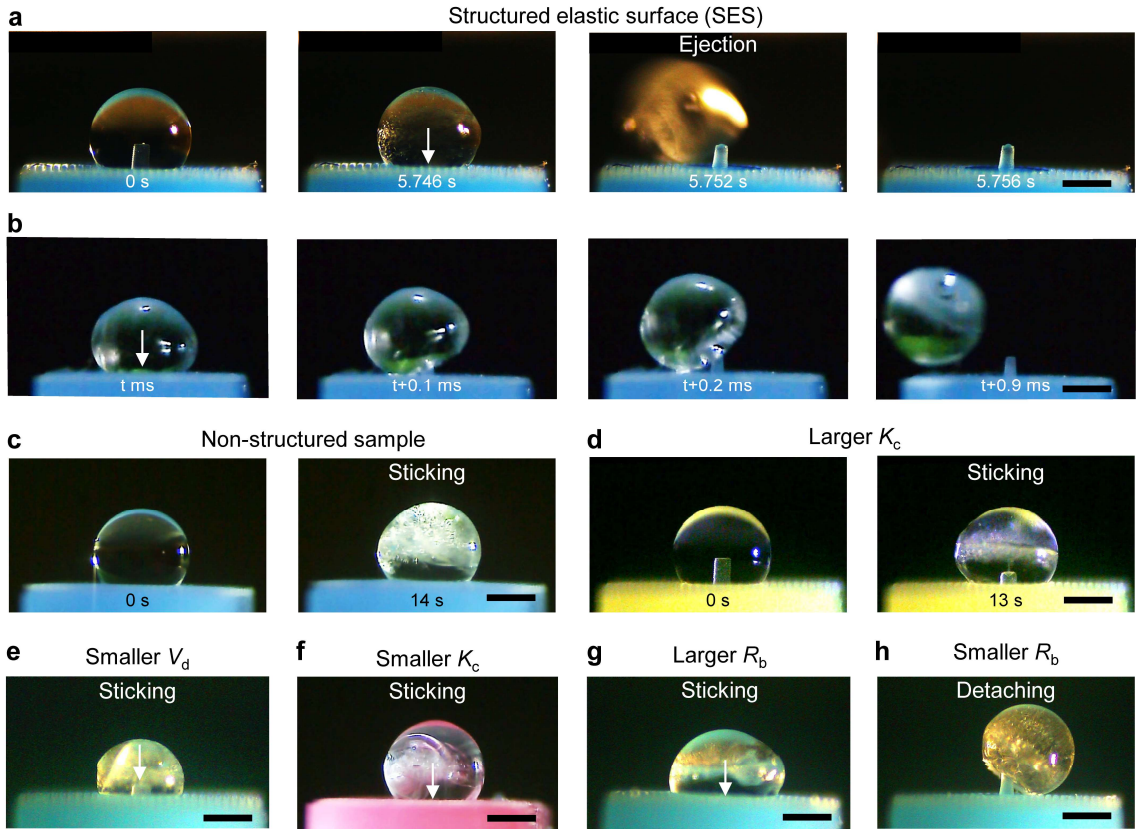

Fig. 2 | Comparison of the freezing droplet behaviors on SES and control samples. a, Spontaneous ejection of a 1-μL freezing droplet on a structured elastic surface (SES) with R_b = 0.5 mm and K_c = 1.7 MPa. **b,** High-speed imaging of the ejection process of a 1-μL freezing droplet on the SES sample used in (**a**). **c-d,** Sticking of 1-μL freezing droplets on (**c**) the non-structured sample without the pillar and (**d**) the stiffer sample with K_c = 5.9 MPa. **e-h,** The dependence of freezing droplet behaviors on droplet size, SES stiffness, and SES geometry. **e,** Sticking of a smaller freezing droplet (0.4 μL) on the SES sample used in (**a**). **f,** Sticking of a 1-μL freezing droplet on the SES with a smaller compressive modulus K_c (0.6 MPa) than the

one used in (**a**). **g,** Sticking of a 1-μL freezing droplet on the SES sample with a larger R_b (0.7 mm) than the one used in (**a**). **h**, Detaching of a 1-μL freezing droplet on the SES sample with a smaller R_b (0.2 mm) than the one used in (**a**). Scale bars, 500 μm. The color of the SES represents the compressive modulus, with yellow corresponding to 5.9 MPa (**d**), blue to 1.7 MPa (**a-c, e, g, h**), and pink to 0.6 MPa (**f**). Arrows indicate the positions of deformed pillars.

We further experimentally evaluate the influences of droplet size, SES stiffness, and SES base size on the spontaneous ejection behaviors of freezing droplets. On the same SES sample used in Fig. 2a, we observed that a smaller droplet (0.4 μL) did not exhibit the spontaneous ejection behavior, but stuck to the SES after freezing (Fig. 2e). Alternatively, on a SES sample with the same structural dimensions but smaller compressive modulus K_c (0.6 MPa), a 1-μL freezing droplet displayed no spontaneous ejection behavior, but stuck to the base surface, as shown in Fig. 2f. Moreover, it was found that the advent of the spontaneous ejection behavior also depends on the base radius (R_b) of the SES because SES samples with the same compressive modulus K_c and pillar as in Fig. 2a failed to eject a 1-μL freezing droplet when the base radius was significantly enlarged or reduced, resulting in droplet sticking or detaching only consequences, respectively (Fig. 2 g and h). These diverse phenomena indicate that the spontaneous ejection of freezing droplets necessitates a proper design of the structural and mechanical properties of the SES in response to droplets of different volumes.

To reveal the underlying mechanism, we further visualize the dynamic interactions between the freezing droplet and the SES. To clearly distinguish the water and ice parts, we added fluorescent dye to the water droplet. When water is frozen into ice with a crystal structure, fluorescent-dye molecules will be expelled out of ice crystals and aggregate together, causing quenching behavior. Because of the aggregation-induced quenching, the ice part becomes colorless, while the water part remains transparent green (Fig. 3a). The transparent water also allows us to examine the dynamics of the pillar inside the droplet. We experimentally confirmed that the addition of fluorescent dyes did not affect the behavior of frozen droplets, as no behavioral differences between dyed and undyed droplets were observed. At the initial freezing stage, the ice shell of the droplet is unstable, easily breaking at the weakest point and then re-freezing upon the cooling by the chilled air, repeatedly until a stable shell is formed. Once the freezing droplet is enclosed by a seamless ice shell, its further volume expansion starts to compress the elastic pillar downwards via the incompressible water medium (Fig. 3a). When the pillar is compressed by about 70% of its original height, the freezing droplet is suddenly

ejected away from the surface within milliseconds at a velocity of ~1 m/s (Fig. 3a).

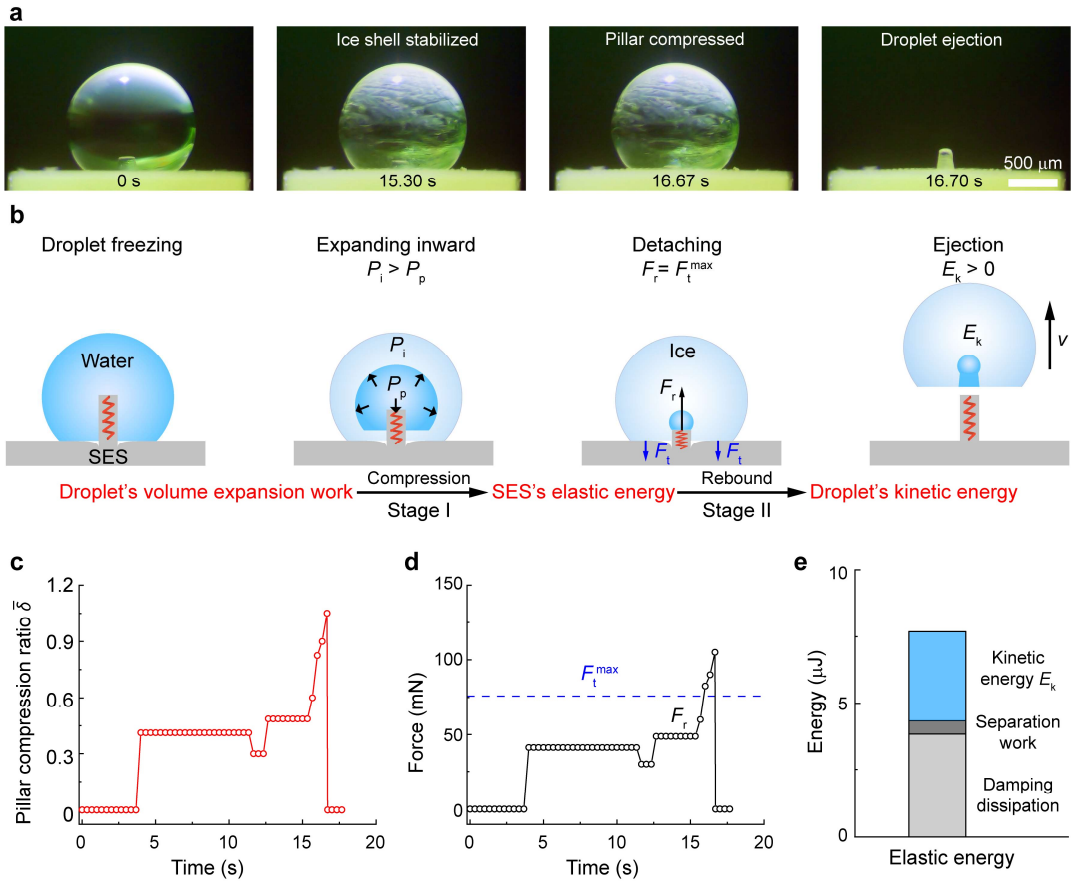

Fig. 3 | Characterization and theoretical modeling of the dynamic interactions between the freezing droplet and the SES. a, Visualization of a 2-μL dyed freezing droplet ejection process on the SES sample with $R_b = 0.5$ mm and $K_c = 5.9$ MPa. **b,** Schematics of the theoretical modeling illustrating the two-stage energy conversion process for freezing droplet ejection by considering the pillar as a spring for energy storage and release. The two-stage energy conversion process, namely stage I, converting the droplet's volume expansion work into SES's elastic energy via pillar compression, and stage II, converting SES's elastic energy into the droplet's kinetic energy via pillar rebound. P_i, the pressure-bearing capacity of the ice shell of the freezing droplet; P_p, the internal pressure of the freezing droplet; F_r, the repelling force generated by the compressed pillar; F_t^{max}, the maximal traction force; E_k, the kinetic energy gained by the freezing droplet. **c,** Real-time pillar compression ratio $\bar{\delta}$ normalized to the initial height of the pillar. **d,** Real-time analysis of the upward repelling force F_r exerted by the compressed pillar and the maximal traction force F_t^{max} on the freezing droplet. **e,** Quantitative analysis of the energy flow for the ejection behavior. In the energy release stage, part of the stored elastic energy E_e is dissipated by the damping and separation work, and the

remaining part is converted into the kinetic energy E_k of the freezing droplet.

The ejection behavior of the freezing droplet on SES results from a two-stage energy conversion process consisting of energy storage (Stage I) and energy release (Stage II). Serving as an energy harvester, the SES first stores the volume expansion work done by the freezing droplet as elastic energy over seconds, and then rapidly releases the stored elastic energy into the droplet's kinetic energy (Fig. 3 a and b). The duration of the energy release (~1 ms) is approximately three orders of magnitude shorter than that of the energy storage (~1000 ms), indicating an amplification of mechanical power output for propelling freezing droplet ejection. The energy storage begins with the downward compression of the spring-like pillar of the SES, caused by the water-to-ice volume expansion in the freezing droplet enclosed by the ice shell (Fig. 3b). The compressed pillar generates a repelling force that grows with further compression. When the repelling force F_r is able to overcome the maximum traction force F_t^{max}, the freezing droplet detaches from the surface, and at the same time, the elastic energy stored in the pillar is rapidly released and partially converted to the droplet's kinetic energy. The amount of kinetic energy E_k ultimately gained by the freezing droplet determines whether the ejection behavior occurs or not. To probe how the droplet size and the stiffness and base size of the SES govern the two-stage energy conversion process, we build a theoretical model by treating the SES as a spring-like mechanical gadget for energy storage and release.

Considering the importance of pillar compression in energy storage and release, we first evaluate the theoretical maximal compression ratio during the freezing process of a given droplet. In stage I of the two-stage energy conversion process, the pillar may undergo multiple cycles of compression and rebound until the droplet detaches from or fully freezes up on the SES (Fig. 3a). The time between two adjacent compression cycles depends on the healing speed of the fractured ice shell, which is related to the cooling conditions, such as the temperature and velocity of the chilled air flow. In a single cycle, the pillar is continuously compressed from its original height until the ice shell of the freezing droplet is fractured by the increased internal pressure owing to the continuous inward volume expansion, or until the freezing droplet detaches (Fig. 3 a and c). As a result, pillar compression is governed by the competition between the pressure-bearing capacity P_i of the ice shell and the internal pressure P_p. We calculate that $P_i = \sigma_i \left[(1-\phi)^{-\frac{2}{3}} - 1\right]$ (see Calculation of the maximal compression ratio of

the pillar, Methods), where σ_i is the fracture strength of ice (~ 0.3 MPa)[36], and the volume fraction of the solidified water ϕ reflects the progression of the freezing process with $\phi = 0$ referring to the non-frozen state and $\phi = 1$ indicating the fully frozen state of the droplet. The internal pressure P_p can be correlated with the pillar's compression ratio through $P_p = K_c\bar{\delta}$, where $\bar{\delta}$ is the compression ratio defined as the downward displacement δ of the pillar tip relative to the original height of the pillar h_p. Because the volume conceded by the descending pillar is equal to the newly expanded volume of the freezing droplet within one cycle, we have $\bar{\delta} = 0.09V_d(\phi_1 - \phi_0)/V_p$, where ϕ_0 and ϕ_1 denote the extent of volume expansion at the starting and ending points of the cycle (Extended Data Fig. 7, see Calculation of the maximal compression ratio of the pillar, Methods), respectively. Note that this volume relationship between droplet expansion and pillar compression only applies to the outside-in freezing directionality where the freezing front acts as a capsule to encapsulate the unfrozen water, and does not apply to other freezing directionalities (top-down, bottom-up, or sideways). In the last cycle, during which $P_i \geq P_p$ is always guaranteed, the maximal compression ratio $\bar{\delta}_{max}$ is attained. Together with the constraint that $\bar{\delta}_{max}$ should be no larger than the unity otherwise draining occurs and the whole process halts, we have

$$\bar{\delta}_{max} = \min\left\{\frac{0.09V_d}{V_p}\left(1.96\mu^{-3/5} - \mu^{-1}\right),\quad 1\right\} \tag{1}$$

where $\mu = 0.09\frac{V_d}{V_p}\frac{K_c}{\sigma_i}$ (See Calculation of the maximal compression ratio of the pillar in the last cycle, Methods). As shown in Extended Data Fig. 8, as V_d/V_p increases, the maximal compression ratio $\bar{\delta}_{max}$ first increases and then reaches a plateau of 1. Additionally, $\bar{\delta}_{max}$ exhibits a negative dependence on K_c under a given V_d/V_p (Extended Data Fig. 8).

Next, we resort to force analysis to determine whether the stored elastic energy in the pillar can be released. The freezing droplet is subject to two directionally opposite forces, including the downward traction force F_t composed of intermolecular adhesion and pressure difference and the upward repelling force F_r exerted by the spring-like pillar via incompressible water as the medium. Here, the gravitational force is found to be 2-3 orders of magnitude lower than the maximum traction force and the repelling force and is thus neglected. The maximum traction

force F_t is estimated to be $F_t^{max} \approx \pi P_{atm}\left(R_b^2 - R_p^2\right)$ (Extended Data Fig. 9, see Calculation of the maximal traction force, Methods), where P_{atm} denotes the atmospheric pressure and is a constant value of 0.1 MPa. The absence of intermolecular adhesion force in F_t^{max} can be attributed to the fact that at the critical detaching moment, a large fraction of the originally-contacting region has deboned and is dominated by the vacuum region. The upward repelling force generated by the spring-like pillar is proportional to the compression ratio through $F_r = \pi R_p^2 K_c \bar{\delta}$, with a maximal value at $\bar{\delta} = \bar{\delta}_{max} \leq 1$. According to the force equilibrium principle, if the maximal F_r can overcome F_t^{max}, the freezing droplet can detach from the base surface to release the stored elastic energy. Otherwise, it will stick to the base surface. As shown in Fig. 3d, when the pillar reaches a compression ratio at which F_r exceeds F_t^{max}, the droplet detachment is successfully triggered. Based on the condition that the maximal F_r should be no smaller than F_t^{max}, we can derive the key parameters that satisfy the force criterion for droplet detachment, expressed as

$$\frac{K_c}{P_{atm}} \geq \frac{R_b^2}{R_p^2} - 1 \tag{2}$$

Thus, we can obtain the lower bound of K_c/P_{atm} as a function of R_b/R_p, above which the repelling force can overcome the traction force, triggering droplet detachment, and thus, the elastic energy can be released.

Achieving the ejection of freezing droplets also requires the attainment of sufficient kinetic energy during the release of the stored elastic energy. In stage II of the two-stage energy conversion process, the released elastic energy E_e has first to pay off the damping dissipation of the pillar E_d and the work for separating the droplet from the pillar E_s. At the critical detaching moment of the droplet, the amount of the elastic energy stored in the spring-like pillar is expressed by $E_e = \frac{K_c}{2} V_p \bar{\delta}_{max}^2 = \frac{K_c}{2} V_p \left[\frac{P_{atm}}{K_c}\left(\frac{R_b^2}{R_p^2} - 1\right)\right]^2$ (see Energy analysis, Methods). The damping dissipation of the pillar elastic energy and the separation work are estimated to be $E_d = (1-\xi)E_e$ and $E_s = P_{atm} V_p \left[1 - \frac{P_{atm}}{K_c}\left(\frac{R_b^2}{R_p^2} - 1\right)\right]$ (see Energy analysis, Methods), respectively, where ξ is the rebound resilience of the pillar, defined as the ratio of energy released from the recovery of deformation to the stored strain energy and measured as ~50% for the PDMS materials (Extended Data Table 1). As a result, the ultimate kinetic energy gained by the freezing droplet is $E_k = \xi E_e - E_s$. For the case shown in Fig. 3a, E_k is calculated as

3.3 μJ and the corresponding energy conversion efficiency is estimated to be 0.435 (Fig. 3e), which explains the occurrence of freezing droplet ejection. In a more general picture, we can get the energy criterion, written as

$$\frac{K_c}{P_{atm}} \leq \frac{1}{2}\xi\left(\frac{R_b^2}{R_p^2}-1\right)^2+\left(\frac{R_b^2}{R_p^2}-1\right) \quad (3)$$

In addition to the force and energy conditions above, another necessary condition for ejection, which is easily neglected, is the consistent presence of liquid water in the ice shell until it separates from the pillar. Otherwise, the ice shell will be stuck to the pillar during the process for the depletion of liquid water even after it detaches from the base. To avoid water depletion, we consider the most conservative scenario, in which the volume expansion of the residual water at the beginning of the last cycle is enough to expel the pillar out from the ice shell, leading to (see Minimum droplet volume for preventing water depletion, Methods)

$$\frac{K_c}{P_{atm}} \leq 1.224\left(\frac{V_d}{V_p}-11.11\right)^{0.732}+2 \quad (4)$$

Combining the preceding force and energy analyses enables us to build a phase diagram for the dynamic behaviors of the freezing droplets on SES (Fig. 4a). In this phase diagram, different volume ratios of the droplet to the pillar are taken: $V_d/V_p = 400, 200, 100, 50$. For each V_d/V_p, the phase diagram shows three regions corresponding to three different droplet behaviors, namely sticking, detaching, and ejection, depending on the radius ratio R_b/R_p and the normalized compressive modulus K_c/P_{atm} of the SES (Fig. 4a). In our experiments, the ratio R_b/R_p was tailored by varying R_b while keeping R_p constant (0.09 mm). For SES with a constant K_c/P_{atm}, an excessively large R_b/R_p makes the droplet fail to overcome the traction force from the surface, resulting in the "sticking" behavior of the droplet. Although an excessively small R_b/R_p enables the droplet to overcome the surface traction, the stored elastic energy in the compressed pillar is insufficient for ejection, resulting in the "detaching" behavior only of the droplet. Only SES with a proper R_b/R_p satisfies both the force and the energy conditions, yielding the "ejection" behavior of the droplet. This accounts for the observations from Fig. 2g and 2h. Alternatively, for SES samples with a given R_b/R_p, the behavior of the freezing droplet can be controlled by tuning the compressive modulus K_c (Fig. 4a). This explains the failure of spontaneous ejection in the case shown in Fig. 2e. Comparing the phase diagrams for different V_d/V_p indicates that the area of the ejection region depends on the droplet volume. The smaller the droplet, the smaller the ejection region. This should be the

reason why a 0.4-μL freezing droplet fails to be ejected by a SES that is able to eject a 1-μL freezing droplet, as shown in Fig. 2d.

To demonstrate the scalability of the SES in ejecting freezing droplets, we also conduct multiple cycles of icing test on SES with 3 × 3 arrays and the smooth sample made of the same materials. In a single cycle, we deposit nine droplets on the two horizontally placed surfaces and measure the mass of residual ice after freezing for 30 s. After six consecutive cycles, we find that the ice residual on SES arrays grows slowly and is only ~33% of that on the control sample (Fig. 4b). This is because, the SES arrays have the ability to shed droplets away by converting the volume expansion work of freezing droplets into kinetic energy, reducing the ice residual on the surface (Fig. 4c).

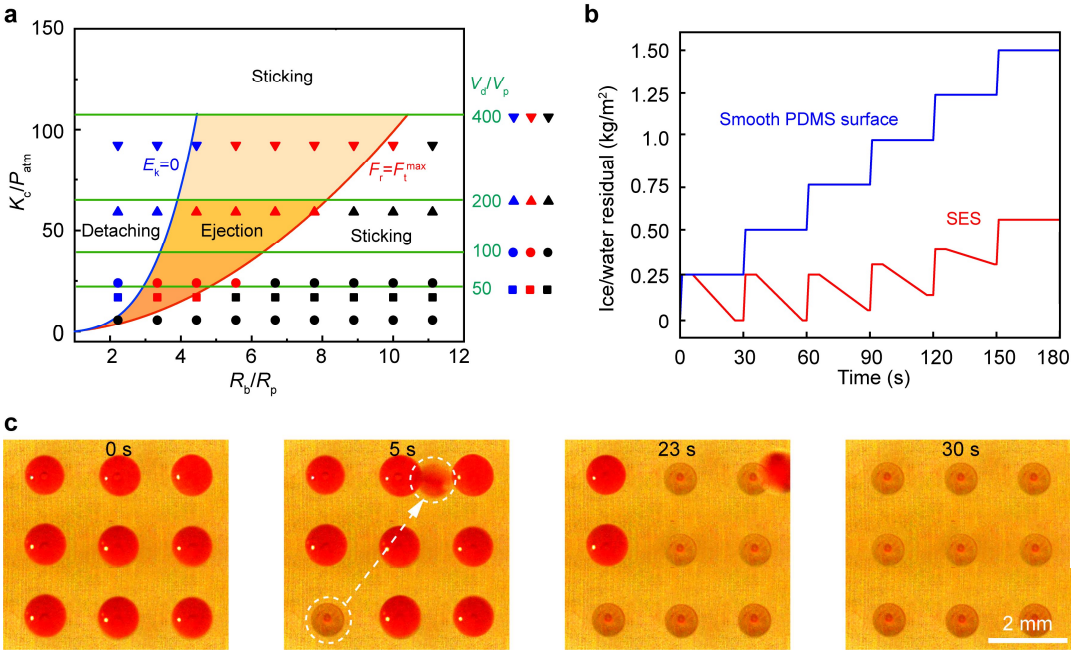

Fig. 4 | Phase diagram of the freezing droplet ejection on SES and practical application. **a,** Phase diagram for the ejection of the freezing droplet on the SES. In this phase diagram, different volume ratios of the droplet to the pillar are taken: $V_d/V_p = 400, 200, 100, 50$. **b,** Comparison of the de-icing performance between the SES arrays and the smooth PDMS surface under multi-cycle icing tests. **c,** Optical images showing one typical cycle of the self-deicing behavior of the SES arrays. The droplets were dyed with fluorescent dye.

In summary, we report a new phenomenon of freezing droplet ejection on the engineered structured elastic surfaces through a two-stage energy conversion process. Mediated by the spring role of the SES, the volume expansion work of freezing droplets is gradually stored as elastic energy at a typical timescale of seconds, while the stored elastic energy is released

within milliseconds. Such a spring-mediated energy transformation gives rise to sufficient kinetic energy for droplet ballistic motion. Owing to the dependence on the directionality of the freezing front, our design may not apply to the non-isothermal freezing ways, such as top-down freezing and bottom-up freezing (Supplementary Video 3), but is suited for common atmospheric-pressure isothermal freezing conditions, such as outdoor winter environments. The volume expansion work-induced droplet ejection deepens our understanding of the multiphase freezing dynamics for anti-icing applications. Our work also demonstrates a new strategy that can efficiently harvest and exploit the largely overlooked volume expansion work of freezing droplets for ballistic motion generation, which could expand the energy conversion phenomena[37] and inspire the development of novel droplet-based energy generators and soft robotic catapults[38] .

References

1 Xu, W. *et al.* A droplet-based electricity generator with high instantaneous power density. *Nature* **578**, 392-396 (2020).

2 Boreyko, J. B. & Chen, C.-H. Self-propelled dropwise condensate on superhydrophobic surfaces. *Phys. Rev. Lett.* **103**, 184501 (2009).

3 Geyer, F. *et al.* When and how self-cleaning of superhydrophobic surfaces works. *Sci. Adv.* **6**, eaaw9727 (2020).

4 Kreder, M. J., Alvarenga, J., Kim, P. & Aizenberg, J. Design of anti-icing surfaces: smooth, textured or slippery? *Nat. Rev. Mater.* **1**, 1-15 (2016).

5 Lv, J., Song, Y., Jiang, L. & Wang, J. Bio-inspired strategies for anti-icing. *ACS nano* **8**, 3152-3169 (2014).

6 Barthlott, W. & Neinhuis, C. Purity of the sacred lotus, or escape from contamination in biological surfaces. *Planta* **202**, 1-8 (1997).

7 Bohn, H. F. & Federle, W. Insect aquaplaning: Nepenthes pitcher plants capture prey with the peristome, a fully wettable water-lubricated anisotropic surface. *Proc. Natl. Acad. Sci. U.S.A.* **101**, 14138-14143 (2004).

8 Wong, T.-S. *et al.* Bioinspired self-repairing slippery surfaces with pressure-stable omniphobicity. *Nature* **477**, 443-447 (2011).

9 Wisdom, K. M. *et al.* Self-cleaning of superhydrophobic surfaces by self-propelled jumping condensate. *Proc. Natl. Acad. Sci. U.S.A.* **110**, 7992-7997 (2013).

10 Kasahara, M. *et al.* Liquid marbles in nature: craft of aphids for survival. *Langmuir* **35**, 6169-6178 (2019).

11 Liu, Y. *et al.* Pancake bouncing on superhydrophobic surfaces. *Nat. Phys.* **10**, 515-519 (2014).

12 Mukherjee, R., Berrier, A. S., Murphy, K. R., Vieitez, J. R. & Boreyko, J. B. How surface orientation affects jumping-droplet condensation. *Joule* **3**, 1360-1376 (2019).

13 Bird, J. C., Dhiman, R., Kwon, H.-M. & Varanasi, K. K. Reducing the contact time of a bouncing drop. *Nature* **503**, 385-388 (2013).

14 Schutzius, T. M. *et al.* Spontaneous droplet trampolining on rigid superhydrophobic surfaces. *Nature* **527**, 82-85 (2015).

15 Richard, D., Clanet, C. & Quéré, D. Contact time of a bouncing drop. *Nature* **417**, 811-811 (2002).

16 Gauthier, A., Symon, S., Clanet, C. & Quéré, D. Water impacting on superhydrophobic macrotextures. *Nat. Commun.* **6**, 8001 (2015).

17 Boinovich, L. B., Emelyanenko, A. M., Ivanov, V. K. & Pashinin, A. S. Durable icephobic coating for stainless steel. *ACS Appl. Mater. Interfaces* **5**, 2549-2554 (2013).

18 Boinovich, L. B. & Emelyanenko, A. M. Anti-icing potential of superhydrophobic coatings. *Mendeleev Commun.* **1**, 3-10 (2013).

19 Graeber, G., Schutzius, T. M., Eghlidi, H. & Poulikakos, D. Spontaneous self-dislodging of freezing water droplets and the role of wettability. *Proc. Natl. Acad. Sci. U.S.A.* **114**, 11040-11045 (2017).

20 Golovin, K., Dhyani, A., Thouless, M. & Tuteja, A. Low–interfacial toughness materials for effective large-scale deicing. *Science* **364**, 371-375 (2019).

21 Golovin, K. & Tuteja, A. A predictive framework for the design and fabrication of icephobic polymers. *Sci. Adv.* **3**, e1701617 (2017).

22 Irajizad, P., Hasnain, M., Farokhnia, N., Sajadi, S. M. & Ghasemi, H. Magnetic slippery extreme icephobic surfaces. *Nat. Commun.* **7**, 13395 (2016).

23 Yang, S. *et al.* Photothermal superhydrophobic copper nanowire assemblies: fabrication and deicing/defrosting applications. *Int. J. Extreme Manuf.* **5**, 045501 (2023).

24 Kim, P. *et al.* Liquid-infused nanostructured surfaces with extreme anti-Ice and anti-frost performance. *ACS Nano* **6**, 6569-6577 (2012).
25 Liu, K. *et al.* Janus effect of antifreeze proteins on ice nucleation. *Proc. Natl. Acad. Sci. U.S.A.* **113**, 14739-14744 (2016).
26 Bi, Y., Cao, B. & Li, T. Enhanced heterogeneous ice nucleation by special surface geometry. *Nat. Commun.* **8**, 15372 (2017).
27 Wu, S. *et al.* Heterogeneous ice nucleation correlates with bulk-like interfacial water. *Sci. Adv.* **5**, eaat9825 (2019).
28 Jung, S. *et al.* Are superhydrophobic surfaces best for icephobicity? *Langmuir* **27**, 3059-3066 (2011).
29 Lambley, H. *et al.* Freezing-induced wetting transitions on superhydrophobic surfaces. *Nat. Phys.* **19**, 649-655 (2023).
30 Knopf, D. A. & Alpert, P. A. Atmospheric ice nucleation. *Nat. Rev. Phys.* **5**, 203-217 (2023).
31 Yang, S. *et al.* Condensation frosting and passive anti-frosting. *Cell Rep. Phys. Sci.* **2** (2021).
32 Chu, F. *et al.* Interfacial ice sprouting during salty water droplet freezing. *Nat. Commun.* **15**, 2249 (2024).
33 Jung, S., Tiwari, M. K., Doan, N. V. & Poulikakos, D. Mechanism of supercooled droplet freezing on surfaces. *Nat. Commun.* **3**, 615 (2012).
34 Mills, A. The freezing bomb. *Physics Education* **45**, 153 (2010).
35 Page, R. M. Sporangium discharge in Pilobolus: A photographic study. *Science* **146**, 925-927 (1964).
36 Raraty, L. & Tabor, D. The adhesion and strength properties of ice. *Proc. Math. Phys. Eng. Sci.* **245**, 184-201 (1958).
37 Luo, D. *et al.* Autonomous self-burying seed carriers for aerial seeding. *Nature* **614**, 463-470 (2023).
38 Zhang, W. *et al.* Honeybee comb-inspired stiffness gradient-amplified catapult for solid particle repellency. *Nat. Nanotechnol.* (2023).
39 Griffith, A. A. VI. The phenomena of rupture and flow in solids. *Phil. Trans. Roy. Soc. Lon. A* **221**, 163-198 (1921).
40 Yao, H. & Zhang, C. A generalized solution to the combo-crack problem—I. Pressure load on crack surface. *J. Mech. Phys. Solids* **159**, 104783 (2022).

Acknowledgments

We acknowledge the financial support from the Research Grants Council of Hong Kong (No. SRFS2223-1S01, No. C1006-20W, No. 11218321, No. 11219219), the National Natural Science Foundation of China (No. 51975502), the Shenzhen Science and Technology Innovation Council (JCYJ20200109143206663), the Innovation and Technology Commission of Hong Kong (GHP/021/19SZ and GHP/092/20GD), the Tencent Foundation through the XPLORER PRIZE and the Meituan Foundation through the Green Tech Award.

Author contributions

Author contributions Z. W. and H. Z. conceived the research. Z. W. and H. Y. supervised the research. H. Z., Y. J., and C. W. prepared the samples. H. Z., Y. J., C. W., and Z. X. designed and carried out the experiments. H. Z., S. Y., S. G., and F. L. analyzed the data. H. Y., H. Z., and W. Z. developed the theoretical modeling. Z. W., H. Y., W. Z., H. Z., and S. W. wrote the manuscript. All authors reviewed and approved the data.

Competing interests

The authors declare no competing interests.

Data availability

All data are available in the main text or the supplementary materials.

Code availability

Code is available from the corresponding authors upon reasonable request.

Methods

Fabrication of SES sample

We fabricated the SES using a simple cast-molding process. First, a mold was made using a projection micro stereolithography-based 3D printing machine (BMF Nano Materials Technology Co., Ltd), and coated with a thin gold layer via a Quorum Coater (Q150TS, Quorum Technologies Inc.) to facilitate the demolding process. We then poured the PDMS (Dow Corning®SYLGARD, PDMS 184) into the mold, degassed it for 30 minutes, and cured it in an oven of 80 ℃ for 2 hours. The SES sample was achieved by demolding and post-curing at 165 ℃ for 48 hours. By changing the mold dimensions, we made SES samples with different pillar radii R_p and base radii R_b. Note that the pillar volume V_p was controlled to be the same for all SES samples, 0.01 μL. We controlled the compressive modulus of SES samples through the base/cross-linker ratios of PDMS. For comparison, we fabricated a non-structured sample using the same processes but with different molds.

Mechanical characterization

We characterized the influences of the base/cross-linker ratio of PDMS on the compressive modulus (K_c) and rebound resilience (ξ). We select five base/cross-linker ratios by weight, including 3, 10, 15, 20, and 25. The compressive modulus (K_c) of these SES samples was measured using an Instron 5567 universal testing machine. To measure the rebound resilience, cylindrical specimens made of PDMS with these five different ratios were tested using a Pendulum rebound tester (UTSTESTER, H029) based on (ASTM D 7121 standard).

Visualization of freezing droplet ejection

To imitate the natural cooling conditions in winter, we built a customized, isothermal environmental chamber and visualized the freezing droplet behavior within. This chamber mainly consisted of a cooling tube and a cooling stage underneath the tube, connected using a heat conductive glue (Hasuncast SG7630) for enhanced heat transfer between them. We placed the SES sample above the cooling tube, with a thermal insulation foam (styrofoam) in between, to prevent direct heat transfer between the SES and the cooling tube. The cooling stage and tube temperatures were controlled at approximately $-15℃$ by the cooling circulator (Julabo, ED-F12) and the Peltier temperature control unit (Dataphysics Instruments, TPC 160). When the ambient air was pumped into the cooling tube, it was cooled down and circulated at 1 m/s within the chamber. As a result, the droplet on the SES was cooled down by the circulated chilly air and started to freeze, just like in natural winter environments. Under such cooling conditions, the droplet freezes inward from its periphery, resulting in the formation of an ice

shell. The freezing process of the droplet and the associated thermal distribution dynamics were recorded using a high-speed camera (MEMRECAM HX-6, Nac) at a frame rate of 500 frames per second (fps) and a thermography camera (FLIR T1020) at a frame rate of 30 fps, respectively. We also filmed the droplet ejection process at a frame rate of 10,000 fps to provide more visual information.

Calculation of the maximal compression ratio of the pillar in the last cycle

The pillar compression is dependent on the competition between the pressure-bearing capacity of the ice shell P_i and the internal pressure P_p. Assuming a compression-and-rebound cycle of the pillar starts at a freezing state with a fraction of the water solidified into ice ϕ_0, the internal pressure and pressure-bearing capacity of the ice shell are given by $P_\mathrm{p} = 0.09K_c\,V_\mathrm{d}(\phi-\phi_0)/V_\mathrm{p}$ and $P_\mathrm{i} \approx \sigma_\mathrm{i}\left[(1-\phi)^{-\frac{2}{3}}-1\right]$, respectively, where ϕ denotes the instant fraction of water solidified into ice with $0 \le \phi_0 \le \phi \le 1$. As shown in Extended Data Fig. 7, the progression of a compression-and-rebound-cycle of the pillar depends on ϕ_0. For a small ϕ_0, P_p would easily reach P_i as ϕ grows, resulting in fracture of the ice shell and terminating the compression-and-rebound cycle of the pillar. After the healing of the fractured ice shell by the cooling environment, a new compression-and-rebound cycle starts from a larger ϕ_0. Such a fracture-and-healing process will repeat until ϕ_0 is greater than a threshold. Subsequently, P_p would not exceed P_i for any $\phi \in [\phi_0, 1]$. Such a threshold of ϕ_0, denoted by ϕ_0^*, can be simply determined by finding the condition when curve $P_\mathrm{p}(\phi)$ becomes a tangent line of curve $P_\mathrm{i}(\phi)$ on the $P/\sigma_i \sim \phi$ plane, as shown in Extended Data Fig. 7. We have

$$\phi_0^* = 1 - 1.96\mu^{-\frac{3}{5}} + \mu^{-1}$$

where μ is a nondimensional parameter $\mu = 0.09\frac{V_\mathrm{d}}{V_\mathrm{p}}\frac{K_\mathrm{c}}{\sigma_\mathrm{i}}$. In this cycle, the maximal compression ratio is achieved when $\phi = 1$, i.e.,

$$\bar{\delta}_\mathrm{max} = 0.09V_\mathrm{d}(1-\phi_0^*)/V_\mathrm{p} = \frac{0.09V_\mathrm{d}}{V_\mathrm{p}}\left(1.96\mu^{-3/5}-\mu^{-1}\right)$$

Meanwhile, $\bar{\delta}_\mathrm{max}$ should be no larger than 1 at which the pillar is fully compressed, leading to

$$\bar{\delta}_\mathrm{max} = \min\left\{\frac{0.09V_\mathrm{d}}{V_\mathrm{p}}\left(1.96\mu^{-3/5}-\mu^{-1}\right),\quad 1\right\}$$

Calculation of the maximal traction force

The downward compression of the pillar under internal pressure of P_p would gradually deform and separate the base of the SES from the freezing droplet, resulting in the formation

and growth of a concave vacuum region with a radius of R_A (Extended Data Fig. 9a). At the same time, the annular contact area between the base and the freezing droplet, characterized by the ratio of R_A to R_B, would decrease. As a result, the downward traction force (F_t) of the droplet is contributed by the contact adhesion (van der Waals force) and the suction induced by the pressure difference between the vacuum region and the atmosphere. Based on the Griffith criterion[39] for crack propagation and the solutions to stress intensity factors in an annular adhesion problem[40], the evolutions of the traction force with respect to the contact area, determined by the ratio of R_A to R_B, are calculated and depicted under different R_b/R_p (Extended Data Fig. 9b). The traction force first increases and then decreases as the contact area reduces, with a maximum value of F_t^{max} dependent on the value of R_b/R_p. We further evaluated the relationship between F_t^{max} and R_b/R_p as $F_t^{max} \approx \pi R_p^2 P_{atm} \Phi_s$, where the nondimensional function $\Phi_s = \left(\frac{R_b}{R_p}\right)^2 - 1$ measures the ratio of the annular wetted area of the base to the sectional area of the pillar (Extended Data Fig. 9c).

Energy analysis

To formulate the energy condition for the occurrence of freezing droplet ejection, we conducted a theoretical analysis to estimate the energy supply and energy consumption, respectively. The energy supply comes from the elastic energy stored in the spring-like pillar. At the impendent moment before the freezing droplet detaches from the SES, the stored elastic energy is calculated as $E_e = \frac{1}{2} F_r \delta_{cr} = \frac{P_{atm}^2 V_p}{2K_c} \Phi_s^2$, where $\delta_{cr} = \frac{P_{atm} h_p}{K_c} \Phi_s$ is the critical compression of the pillar at which the repelling force F_r is equal to the maximal traction force F_t^{max}. The inherent damping dispassion of the pillar accounts for $(1-\xi)E_e$. Here, ξ denotes the rebound resilience of the pillar, which was measured to be around 50% for the PDMS we applied (Extended Data Table 1). After detaching from the SES, the freezing droplet remains in contact with the pillar. When the droplet separates from the pillar, a negative pressure ($-P_{atm}$) will be generated inside, resulting in a suction force $\pi R_p^2 P_{atm}$ in between. The separation work is estimated as $E_s = \pi R_p^2 P_{atm}(h_p - \delta_{cr}) = V_p P_{atm}\left[1 - \frac{P_{atm}}{K_c}\Phi_s\right]$. As a result, the kinetic energy gained by the freezing droplet for ejection is calculated as $E_k = \xi E_e - E_s$.

Minimum water droplet volume for preventing water depletion

To avoid the running out of liquid water during the freezing process, we consider the most

conservative scenario, in which the volume expansion of the residual water at the beginning of the last cycle is enough to expel the pillar out from the ice shell. That is,

$$0.09V_{\mathrm{d}}(1-\phi_0^*) \geq V_{\mathrm{p}}$$

Substituting $\phi_0^* = 1 - 1.96\mu^{-\frac{3}{5}} + \mu^{-1}$ into above expression, we have

$$0.09V_{\mathrm{d}}\left(1.96\mu^{-3/5} - \mu^{-1}\right) \geq V_{\mathrm{p}}$$

Recalling $\mu = 0.09\frac{V_{\mathrm{d}}}{V_{\mathrm{p}}}\frac{K_{\mathrm{c}}}{\sigma_{\mathrm{i}}}$, above inequality can be rewritten as

$$\frac{V_{\mathrm{d}}}{V_{\mathrm{p}}} \geq 2.07\left(\frac{K_{\mathrm{c}}}{\sigma_{\mathrm{i}}}\right)^{-1}\left[\left(\frac{K_{\mathrm{c}}}{\sigma_{\mathrm{i}}}+1\right)\right]^{5/2}$$

This gives rise to a minimum requirement for the initial volume of the water droplet to prevent water depletion during the whole process before the separation of the ice shell and pillar. By some basic mathematical manipulations, the relationship between $\frac{V_{\mathrm{d}}}{V_{\mathrm{p}}}$ and $\frac{K_{\mathrm{c}}}{\sigma_{\mathrm{i}}}$ given by the above inequality can also be rewritten in an inverse form as

$$\frac{K_{\mathrm{c}}}{\sigma_{\mathrm{i}}} \leq 0.408\left(\frac{V_{\mathrm{d}}}{V_{\mathrm{p}}} - 11.11\right)^{0.732} + 0.667$$

By multiplying both sides of the above inequality by $\sigma_{\mathrm{i}}/P_{\mathrm{atm}}$, which is presumably taken as $\sigma_{\mathrm{i}}/P_{\mathrm{atm}} = 3$, we can get

$$\frac{K_{\mathrm{c}}}{P_{\mathrm{atm}}} \leq 1.224\left(\frac{V_{\mathrm{d}}}{V_{\mathrm{p}}} - 11.11\right)^{0.732} + 2$$

Supplementary Figure

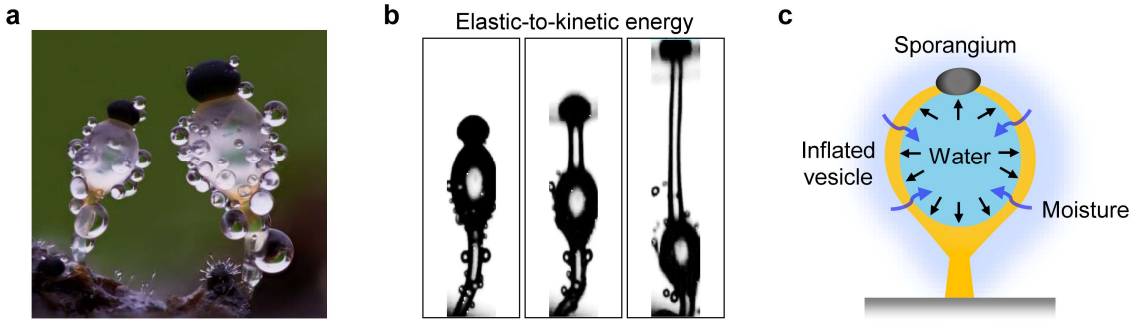

Extended Data Fig. 1 | Energy conversion for spore dispersal in the fungus (zygomycete *Pilobolus kleinii*). a, Photograph of the fungus (zygomycete *Pilobolus kleinii*). **b,** Snapshots showing the spore dispersal behavior of the fungus driven by the conversion of elastic-to-kinetic energy. **c,** Schematics of the mechanism of the energy conversion process in the fungus.

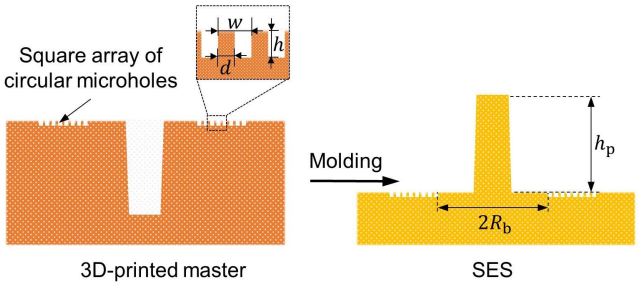

Extended Data Fig. 2 | Schematic illustration of the fabrication process of the SES. We fabricate the SES using the cast-molding method based on the 3D-printed masters. Here d and h, the diameter and height of the micropattern; w, the center-to-center spacing between the micro patterns; h_p, the height of the pillar; R_b, the radius of the smooth base.

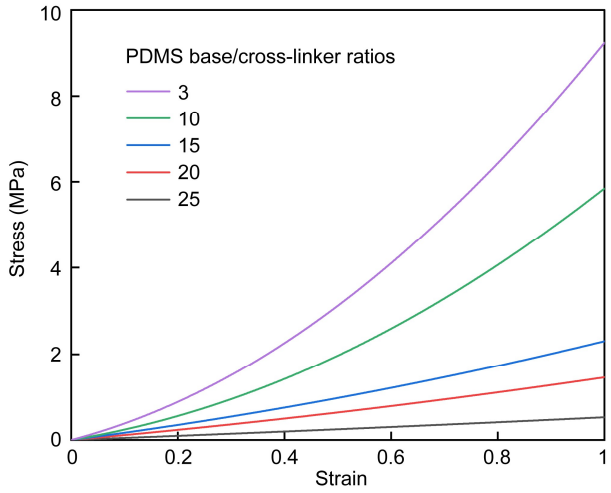

Extended Data Fig. 3 | The compression tests of SES made of PDMS with different base/cross-linker ratios by weight. The compressive modulus (K_c) equals the stress value when the strain reaches 1.

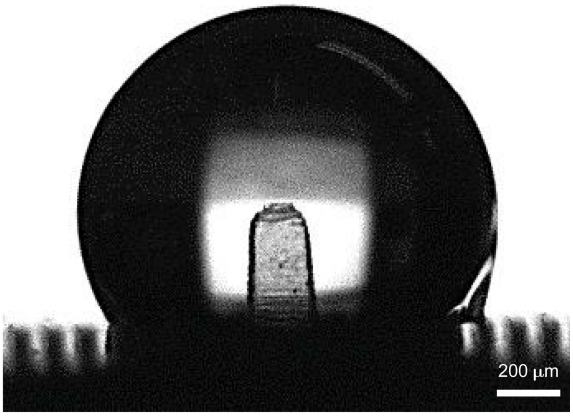

Extended Data Fig. 4 | Contact angle of the water droplet sitting on the SES.

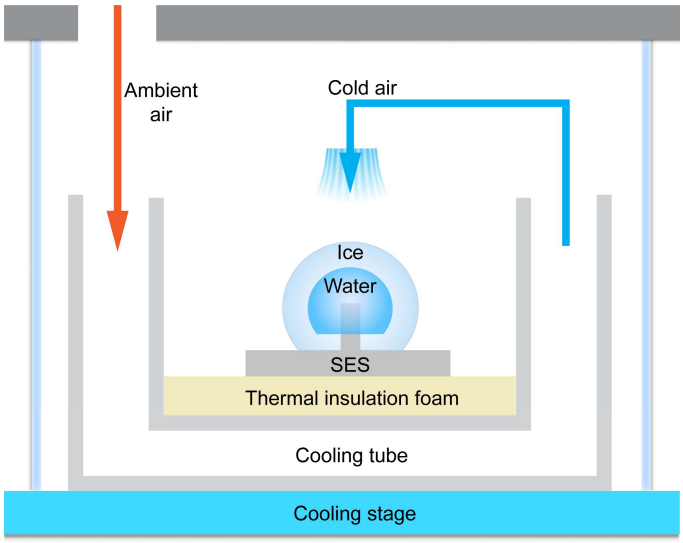

Extended Data Fig. 5 | Schematics of the experimental setup for the freezing droplet ejection. The droplet on the SES is cooled down by the chilly air circulated at ~1 m/s within an isothermal environmental chamber (~−15℃).

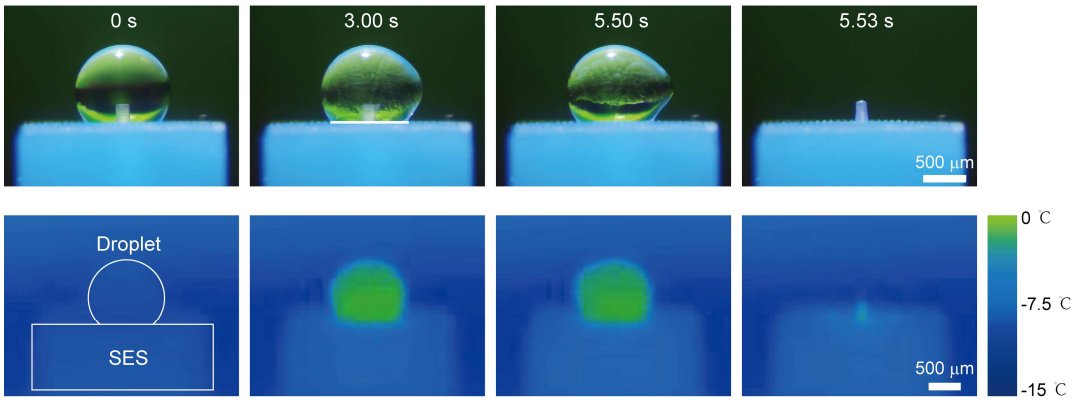

Extended Data Fig. 6 | Optical and thermographic imaging of the water droplet freezing process on the SES sample. The uniform temperature distribution within the SES illustrates that the droplet is cooled down by the circulated chilly air in the isothermal chamber.

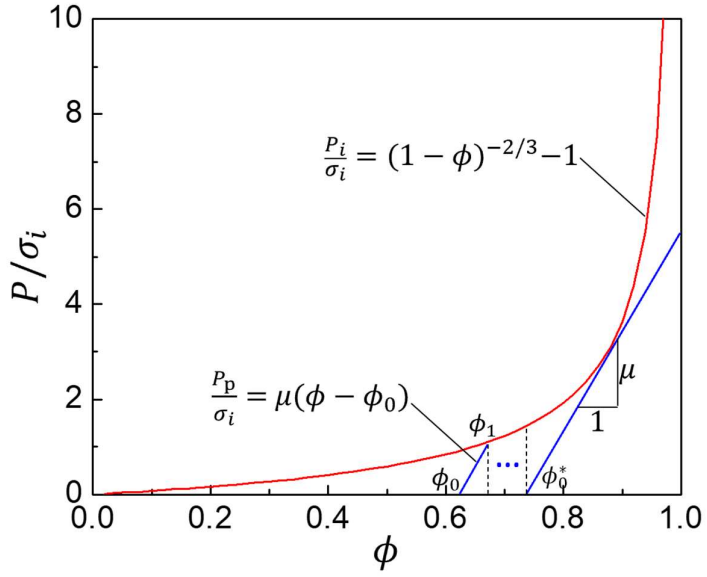

Extended Data Fig. 7 | The dynamic competition between the pressure-bearing capacity of the ice shell P_i and the internal pressure P_p. Here ϕ_0^* denote the critical value of the fraction of the solidified water (ϕ_0), whereby the ice shell will not fracture in the subsequent compression-rebound cycle.

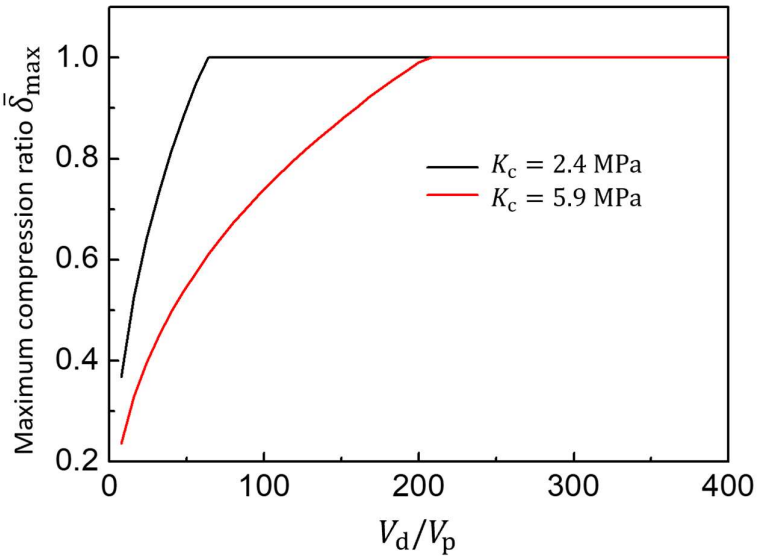

Extended Data Fig. 8 | The maximal compression ratio $\bar{\delta}_{max}$ as a function of the volume ratio of a droplet to a pillar V_d/V_p under different K_c. It can be found that $\bar{\delta}_{max}$ first increases as V_d/V_p increases and then reaches a plateau of 1. Here, the fracture strength of ice is taken as $\sigma_i = 0.3$ MPa. Additionally, $\bar{\delta}_{max}$ exhibits a negative dependence on K_c. For a given

V_d/V_p, the higher K_c the lower $\bar{\delta}_{max}$.

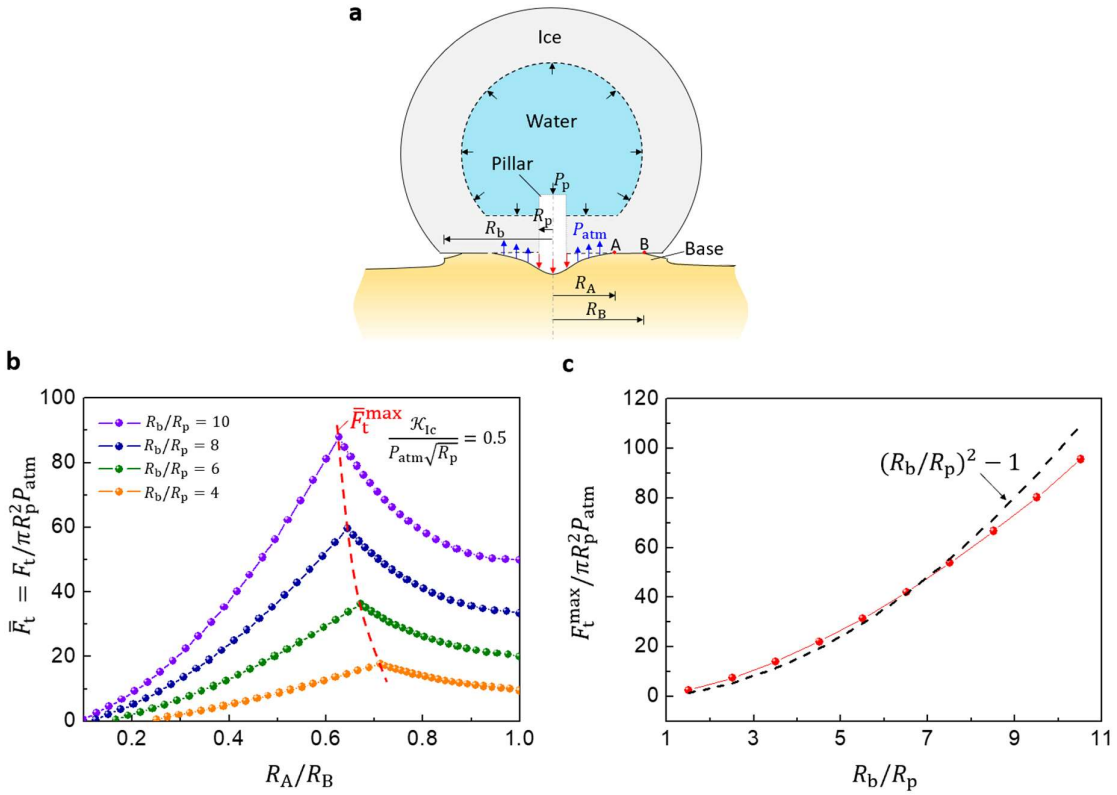

Extended Data Fig. 9 | Theoretical modeling for determining the maximum traction force between the freezing droplet and the base. a, Schematics showing a snapshot of the separation process between a freezing droplet and the base of SES. **b,** The variation of the normalized traction force ($F_t/\pi R_p^2 P_{atm}$) with the radius ratio between the inner and outer contact edges for different R_b/R_p. Here, the normalized fracture toughness of the interface was assumed as $\frac{\mathcal{K}_{Ic}}{P_{atm}\sqrt{R_p}} = 0.5$ with $\mathcal{K}_{Ic}$ being the critical stress intensity factor for interfacial delamination. **c,** Dependence of the maximum normalized traction force (the peak values on the curves in **b**) on the radius ratio between the base and pillar (R_b/R_p).

Extended Data Table 1 | The mechanical characterization of the SES made of PDMS with different base/cross-linker ratios by weight.

PDMS base/cross-linker ratio (by weight)	Compressive modulus K_c (MPa)	Rebound resilience ξ
3	9.2	55%
10	5.9	51%
15	2.4	44%

20	1.7	45%
25	0.6	44%

Supplementary Video 1 | The ejection behavior of the freezing water droplet on the SES inspired by the fungus under isothermal freezing conditions.

Supplementary Video 2 | Synchronous thermographic and optical imaging of the freezing process of a water droplet on the SES. The uniform temperature distribution within the SES illustrates that the droplet is cooled down by the circulated chilly air in the isothermal chamber.

Supplementary Video 3 | Absence of ejection behavior of the water droplet on the SES under bottom-up freezing conditions.